Axillary region level III

(c)

Fig. 3. (Cont'd).

tients. In both CTIT and MTIT planning, the breast tissue was sufficiently irradiated.

The entire axillary lymph node region, as well as the breast tissue, was irradiated by MTIT. The axillary lymph node regions at Levels I, II, and III were irradiated with 84–100% (median, 94.5%), 59–100% (median, 89%), and 70–100% (median, 89.5%) volumes, respectively, at >70% of the isocenter dose for patients treated with MTIT. The areas irradiated with MTIT at each axillary level were much wider than those irradiated with CTIT. Breast tissue is the only target in planning CTIT, and low control rates for the axillary lymph node region have generally been reported

Table 2. Irradiated heart volume in left breast cancer patients

Heart volume (cm³)	MTIT (n = 14)			CTIT (n = 11)		
	80%	50%	30%	80%	50%	30%
0–10	13	9	6	8	5	4
11–30	1	4	6	3	4	5
31	0	1	2	0	2	2

Abbreviations as in Table 1.
Percentages represent radiation dose.

(16–18). Goodman et al. (19) reported the Level I area was well covered, and Aristei et al. (14) reported the Level I and II areas were not entirely covered by CTIT. Radiation doses of 45–50 Gy have been reported to provide excellent control rates for subclinical lymph node involvement (20). All patients in this study received 50 Gy in 25 fractions of external beam RT. Furthermore, 70% of the isocenter dose was 35 Gy (1.4 Gy/fraction), which appeared to be an insufficient dose to control axillary lymph node recurrence. However, Withers et al. (21) stated that the dose–response curve for control of subclinical metastases is linear, and local control of the axillary region can, to some extent, be expected at doses of <45–50 Gy. Three-dimensional conformal RT or intensity-modulated RT is anticipated to be able to handle this problem of underdosing. Long follow-up is required to determine the true benefit of MTIT.

Areas near the edges of the radiation field, especially the dorsal areas at Levels I–III and the cranial areas at Levels II and III, were underdosed. Lymph node failure in the supraclavicular region, which cannot be clearly distinguished from the Level III cranial area, was seen in a few cases. However, lymph node failure in the other underdosed areas was rare. The radiation field in MTIT cannot be expanded

for dorsal direction to achieve a sufficient field margin, because the extended field would involve a larger lung volume and result in greater complication rates. Careful and accurate planning is needed at every radiation session to reduce the risk of underdosing the marginal lymph node areas and to minimize the lung volume involved.

The lung volume irradiated with MTIT was small but significantly larger than that irradiated with CTIT. Radiation pneumonitis and fibrosis have been thoroughly discussed, and reducing the lung volume irradiated must be given the highest priority to avoid these complications (22, 23). The frequency of pneumonitis varies from 0% up to 50%, depending on the radiation technique used (24–33). However, Lingos et al. (34) reported that the amount of irradiated lung volume was not associated with radiation pneumonitis within a limited range of irradiated lung volumes, defined as a central lung distance <3 cm. Lind et al. (33) reported a central lung distance >2.5 cm to be directly related to the incidence of lung complications and showed that 50% of patients had pulmonary complications with internal mammary node and supraclavicular field treatment along with the tangential breast field. We planned both CTIT and MTIT with a central lung distance of <2.5 cm

and no symptomatic pulmonary complications had occurred at 1 year after treatment.

Rutqvist et al. (35, 36) reported a high dose of ^{60}Co radiation to be associated with a high risk of cardiac complications. However, when an electron beam was used for the internal mammary node field, no complications occurred. It was concluded that cardiac problems could be avoided by the use of proper field arrangements and reducing the radiation dose. In this series, the irradiated heart volume was negligible in right-sided breast cancer patients and was also very small in left-sided breast cancer patients. Cardiac toxicity would not be produced by MTIT, as reported for CTIT (32, 37).

CONCLUSION

Our results suggest that the breast tissue was sufficiently irradiated with both CTIT and MTIT planning, that axillary lymph node areas irradiated by MTIT were much wider than those irradiated by CTIT at all levels, that the lung and heart volumes irradiated by MTIT were small, and that pulmonary and cardiac toxicity may not be increased compared with the results reported thus far.

REFERENCES

1. Cady B. The need to reexamine axillary lymph node dissection in invasive cancer. Cancer 1994;73:505–508.
2. Haffty BG, Ward B, Pathare P, et al. Reappraisal of the role of axillary lymph node dissection in the conservative treatment of breast cancer. J Clin Oncol 1997;15:691–700.
3. Dent DM. Axillary lymphadenectomy for breast cancer: Paradigm shifts and pragmatic surgeons. Arch Surg 1996;131:1125–1127.
4. Cady B, Stone MD, Wayne J. New therapeutic possibilities in primary invasive breast cancer. Ann Surg 1993;218:338–349.
5. Halverson KJ, Taylor ME, Perez CA, et al. Regional nodal management and patterns of failure following conservative surgery and radiation therapy for stage 1 and 2 breast cancer. Int J Radiat Oncol Biol Phys 1993;26:593–599.
6. Hoskin PJ, Rajan B, Ebbs S, et al. Selective avoidance of lymphatic radiotherapy in the conservative management of early breast cancer. Radiother Oncol 1992;25:83–88.
7. Kuznetsova M, Graybill JC, Zusag TW, et al. Omission of axillary nymph node dissection in early-stage breast cancer: Effect on treatment outcome. Radiology 1995;197:507–510.
8. Ogawa Y, Nishioka A, Inomata T, et al. Conservation treatment intensified with tamoxifen and CAF chemotherapy without axillary dissection cancer patients with clinically-negative axillary nodes. Oncol Rep 1999;6:801–805.
9. Wong JS, Recht A, Beard CJ, et al. Treatment outcome after tangential radiation therapy without axillary dissection in patients with early-stage breast cancer and clinically negative axillary nodes. Int J Radiat Oncol Biol Phys 1997;39:915–920.
10. Harlow SP, Krag DN. Sentinel lymph node—Why study it: Implications of the B-32 study. Semin Surg Oncol 2001;20:224–229.
11. Muren LP, Maurstad G, Hafslund R, et al. Cardiac and pulmonary doses and complication probabilities in standard and conformal tangential irradiation in conservative management of breast cancer. Radiother Oncol 2002;62:173–183.
12. Hong L, Hunt M, Chui C, et al. Intensity-modulated tangential

beam irradiation of the intact breast. Int J Radiat Oncol Biol Phys 1999;44:1155–1164.
13. Kong FM, Klein EE, Bradley JD, et al. The impact of central lung distance, maximal heart distance, and radiation technique on the volumetric dose of the lung and heart for intact breast radiation. Int J Radiat Oncol Biol Phys 2002;54:963–971.
14. Aristei C, Chionne F, Marsella AR, et al. Evaluation of level I and II axillary nodes included in the standard breast tangential fields and calculation of the administered dose: Results of a prospective study. Int J Radiat Oncol Biol Phys 2001;51:69–73.
15. Takeda A, Shigematsu N, Kondo M, et al. The modified tangential irradiation technique for breast caner: How to cover the entire axillary region. Int J Radiat Oncol Biol Phys 2000;46:815–822.
16. Krasin M, McCall A, King S, et al. Evaluation of a standard breast tangent technique: A dose-volume analysis of tangential irradiation using three-dimensional tools. Int J Radiat Oncol Biol Phys 2000;47:327–333.
17. Smitt MC, Goffinet DR. Utility of three-dimensional planning for axillary node coverage with breast-conserving radiation therapy: Early experience. Radiology 1999;210:221–226.
18. Botnick M, McCormick Hunt M, et al. Are the axillary lymph nodes treated by standard tangent breast fields? [Abstract]. Int J Radiat Oncol Biol Phys 1998;42:245.
19. Goodman RL, Grann A, Saracco P, et al. The relationship between radiation fields and regional lymph nodes in carcinoma of the breast. Int J Radiat Oncol Biol Phys 2001;20:99–105.
20. Montague ED, Tapley ND, Baker JL. Radiotherapy in the management of nondisseminated breast cancer. In: Fletcher GH, editor. Textbook of radiotherapy, 3rd ed. Philadelphia: Lea & Febiger, 1980: p. 527–579.
21. Withers HR, Peters LJ, Taylor JMG. Dose-response relationship for radiation therapy of subclinical disease. Int J Radiat Oncol Biol Phys 1995;31:353–359.
22. Hardman PD, Tweeddale PM, Kerr GR, et al. The effect of

pulmonary function of local and loco-regional irradiation for breast cancer. *Radiother Oncol* 1994;30:33–42.

23. Kimsey FC, Mendenhall NP, Ewald LM, *et al.* Is radiation treatment volume a predictor for acute and late effect on pulmonary function? A prospective study of patients treated with breast-conserving surgery and postoperative irradiation. *Cancer* 1994;73:2549–2555.

24. Read PE, Ash DV, Thorogood J, *et al.* Short term morbidity and cosmesis following lumpectomy and radical radiotherapy for operable breast cancer. *Clin Radiol* 1987;38:371–373.

25. Rothwell RI, Kelly SA, Joshlin CAF. Radiation pneumonitis in patient treated for breast cancer. *Radiother Oncol* 1985;4: 9–14.

26. Lind BK, Brahme A. Optimization of radiation therapy dose distributions using scanned electron and photon beams and multileaf collimators. In: Bruinvis IAD, van der Giessen PH, van Kleffens HJ, Wittkämper FW, editors. Proceedings of the Ninth International Conference on the Use of Computers in Radiation Therapy. Scheveningen, The Netherlands; 1987. p. 227–330.

27. Rotstein S, Lax I, Svane G. Influence of radiation therapy on the lung tissue in breast cancer patients: CT-assessed density changes and associated symptoms. *Int J Radiat Oncol Biol Phys* 1990;18:173–180.

28. Polansky SM, Ravin CE, Prosnitz LR. Pulmonary changes after primary irradiation of early breast carcinoma. *AJR Am J Roentgenol* 1980;134:101–105.

29. Halverson KJ, Leung TC, Pellet JB, *et al.* Study of treatment variation in radiotherapy of head and neck tumors using a fiber-optic radiotherapy imaging system. *Int J Radiat Oncol Biol Phys* 1991;21:1327–1336.

30. Markiewicz DA, Scultz DJ, Haas JA, *et al.* The effects of sequence and type of chemotherapy and radiation therapy on cosmesis and complications after breast conservation therapy. *Int J Radiat Oncol Biol Phys* 1996;35:661–668.

31. Pierce SM, Recht A, Lingos TI, *et al.* Long-term radiation complications following conservative surgery (CS) and radiation therapy (RT) in patients with early stage breast cancer. *Int J Radiat Oncol Biol Phys* 1992;23:915–923.

32. Fowble B, Fein DA, Hanlon AL, *et al.* The impact of tamoxifen on breast recurrence, cosmesis, complications, and survival in estrogen receptor-positive early-stage breast cancer. *Int J Radiat Oncol Biol Phys* 1996;35:669–677.

33. Lind PARM, Gagliardi G, Wennberg B, *et al.* A descriptive study of pulmonary complications after postoperative radiation therapy in node-positive stage II breast cancer. *Acta Oncol* 1997;36:509–515.

34. Lingos TI, Recht A, Vicini F, *et al.* Radiation pneumonitis in breast cancer patients treated with conservative surgery and radiation therapy. *Int J Radiat Oncol Biol Phys* 1991;21:355–360.

35. Rutqvist LE, Johansson H. Mortality by laterality of primary tumour among 55 000 breast cancer patients from Swedish cancer registry. *Br J Cancer* 1990;61:866–868.

36. Rutqvist LE, Lax I, Fornander T, *et al.* Cardiovascular mortality in randomized trial of adjuvant radiation therapy versus surgery alone in primary breast cancer. *Int J Radiat Oncol Biol Phys* 1992;22:887–896.

37. Das IJ, Cheng EC, Freedman G, *et al.* Lung and heart dose volume analyses with CT simulator in radiation treatment of breast cancer. *Int J Radiat Oncol Biol Phys* 1998;42:11–19.

CASE REPORT

Radiation Therapy for Idiopathic Orbital Myositis: Two Case Reports and Literature Review

Koichi Isobe,* Takashi Uno,* Hiroyuki Kawakami,* Naoyuki Ueno,* Tetsuya Kawata,* Hideki Abe,** Katsuyuki Minowa,** Shuichi Yamamoto,** and Hisao Ito*

We report two cases of idiopathic orbital myositis treated with radiation therapy (RT). Both patients visited our hospital with complaints of orbital pain on eye movement and eyelid swelling. There was no history of thyroid disease or trauma, and no signs of infection, neoplasm, or collagen disease. The laboratory investigations, including a thyroid function test, showed no abnormalities in either woman. They were initially treated with a combination of corticosteroids (CS) and nonsteroidal anti-inflammatory drugs (NSAIDs), however, they became dependent on or refractory to oral CS therapy, and received 20 Gy in 10 fractions of RT to the orbit. Their symptoms decreased immediately, and both patients were able to reduce the dosage of oral CS after RT. One patient could completely withdraw oral CS thereafter. However, they both experienced recurrence at eight months after RT, and have been receiving oral CS to control their symptoms. RT at doses of 20 Gy in 10 fractions for patients with idiopathic orbital myositis appears to be effective in palliating symptoms, but long-term control is not satisfactory.

Key words: idiopathic orbital myositis, radiation therapy, steroid

INTRODUCTION

IDIOPATHIC ORBITAL MYOSITIS IS AN INFLAMMATION OF the extraocular muscles. It is clinically characterized by orbital pain on eye movement and restriction of ocular motility with normal thyroid function tests. Orbital myositis is usually treated with oral corticosteroids (CS). Most patients respond well to initial treatment with these drugs, however, a significant number of patients experience recurrences. When recurrences occur, patients receive repeated courses of CS therapy, which are usually effective in relieving symptoms. However, long-term CS therapy may lead to serious complications, and some patients become intolerant or refractory to these treatments. In such cases, low-dose radiation therapy (RT) has been proved to be a valuable alternative to CS. RT for idiopathic orbital myositis was first described by Sergott et al. in 1981, and 17 cases have

been reported since then.[1-7] Some concluded that RT was effective,[1,3,4,6] but others did not,[2,5,7,8] and the efficacy of RT for orbital myositis has yet to be established. We report two patients with orbital myositis who received 20 Gy of RT, and review the literature.

CASE REPORTS

Two female patients with a diagnosis of idiopathic orbital myositis were the subjects of our study. The patients' characteristics are summarized in Table 1. Both patients visited our hospital with complaints of pain on eye movement and eyelid swelling. Case 2 also complained of adduction disorder. There was no history of thyroid disease or trauma, and no signs of infection, neoplasm, or collagen disease. Neither had a family history of thyroid disease. The laboratory data, including a thyroid function test, showed no abnormalities in either woman. Magnetic resonance imaging (MRI) showed left inferior rectus muscle swelling in case 1, and right medial and lateral rectus muscle swellings in case 2 (Fig. 1).

They were initially treated with a combination of CS and nonsteroidal anti-inflammatory drugs (NSAIDs), which resolved their symptoms immediately. However, attempts to reduce the dosage of prednisolone were

Table 1. Patient characteristics

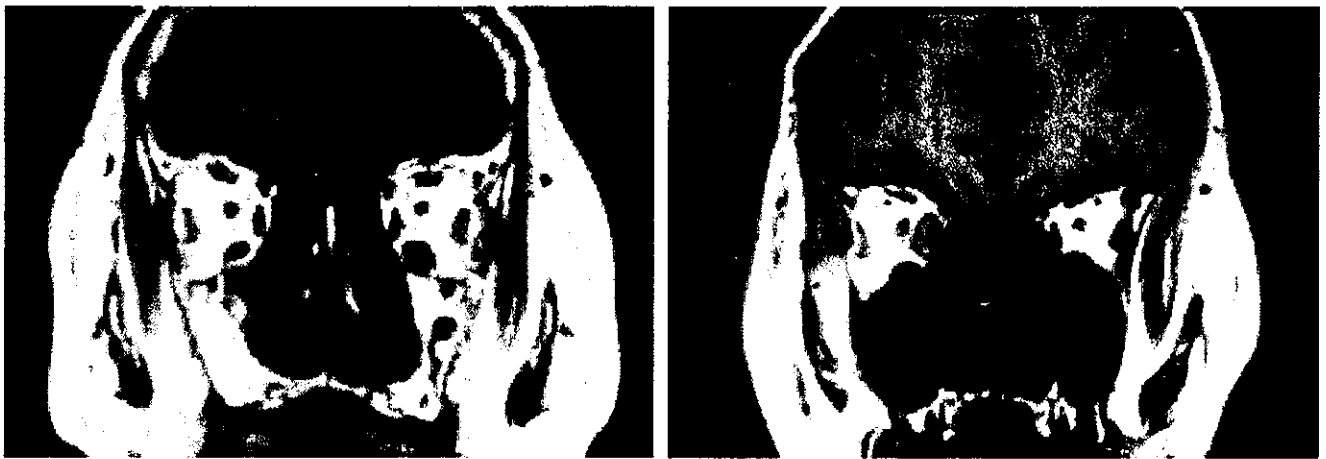|	Case 1	Case 2
Age	50	33
Sex	Female	Female
Thyroid function test		
FT3 (1.71-3.71 pg/ml)	2.60	1.44
FT4 (0.70-1.48 ng/dl)	0.82	1.10
TSH (0.350-4.940 μIU/ml)	0.598	1.082
Symptom	Orbital pain on eye movement	Orbital pain on eye movement
	Eyelid swelling	Eyelid swelling
		Diplopia
Involved muscles	Inferior rectus	Lateral rectus
		Medial rectus

Fig. 1.
A: Case 1; T1-weighted coronal images show left inferior rectus muscle swelling.
B: Case 2; T1-weighted coronal images show right medial and lateral rectus muscle swellings.

A | B

hampered by the reappearance of symptoms. They became dependent on oral CS therapy thereafter, and received RT.

They received 20 Gy in 10 fractions of RT to the affected side of the orbit. Their symptoms decreased immediately, and both patients were able to reduce the dosage of oral CS after RT. Case 1 could completely withdraw oral CS thereafter. However, they both experienced recurrence of symptoms at eight months after RT, and they have been receiving oral CS to control their symptoms.

DISCUSSION

Idiopathic orbital myositis is a rare inflammatory disease affecting the extraocular muscles. It is usually treated with oral CS, however, in some instances, it is also treated with NSAIDs. Which of these treatments is more

effective remains to be determined. Some have recommended initial treatment with three weeks of NSAIDs such as ibuprofen,[6] but others have recommended oral CS.[3,7,8] RT has been employed in cases refractory to or dependent on CS, however, its rationale for improving symptoms and its efficacy are unclear. Moreover, the total dose to be delivered and volume to be treated have not been clarified. We summarize the results of RT for orbital myositis in Table 2.

In 1981, Sergott et al. first reported the efficacy of low-dose (10 to 20 Gy) RT in 19 patients with idiopathic orbital pseudotumors.[1] Of these 19 patients, one met the criteria for idiopathic orbital myositis. They described that she had received 16 Gy of RT and was disease free at 27 months' follow-up. Weinstein et al. also reported that three patients who had become refractory to CS were successfully treated with RT.[3] Sekhar et al. reported a patient with myositis who received 25 Gy of RT with

Table 2. The results of radiation therapy (literature review)

Author	No. of Pts	Indication for RT	Dose (Gy)	Results	Recurrence	Progression-free interval (mo)
Sergott[1]	1	CS dependence	16	Cured	No	27
Slavin[2]	1	CS intolerance	16	Improved	Yes	Soon after RT
Weinstein[3]	3	CS refractory	30	Improved (3)	NR	
Sekhar[4]	1	NR	25	Cured	No	24
Bessant[5]	1	CS refractory	20	Ineffective	–	
Mannor[6]	4	CS refractory	20-25	Cured (2) Ineffective (2)	NR	
Mombaerts[7]	6	CS refractory or CS intolerance	20	Cured (6)	Yes (6)	0.5-106
Current	2	CS dependence	20	Improved (2)	Yes (2)	

No.: number, Pts: patients, CS: corticosteroid, NR: not reported, RT: radiation therapy, mo: months
Numbers in parentheses indicate number of patients.

systemic CS therapy,[4] and recovered completely after the treatment.

Mannor et al. reported that four patients with recurrent episodes of myositis received low-dose (20 to 25 Gy) RT.[6] Although the details are unknown, they reported that two responded to the RT, and the remaining two required surgical intervention. A report from Miami University described a 27-year-old woman who received 16 Gy of RT due to CS intolerance.[2] Her symptoms resolved quickly after the RT, however, she experienced recurrence and received a second course of RT (14 Gy). Bessant and Lee reported a CS-refractory patient who received 20 Gy of RT and did not respond to it.[5] Mombaerts and Koornneef reported six patients who received 20 Gy of RT due to a refractory response or intolerance to CS.[7] Although RT resolved the symptoms in the six patients, recurrences continued to occur within a mean period of 2.7 years (range, 0.5 months to 8.8 years), and they concluded that 20 Gy of RT appeared ineffective for stopping recurrent orbital myositis.

As far as we know, 19 patients have received RT for orbital myositis, including the current two cases. The indication for RT was refractory response to or dependency on CS, and was common among the investigators. Of the 19 patients, 16 responded to RT and the remaining three did not. However, nine responders experienced recurrences. The present two cases also responded well to RT and experienced recurrences. Furthermore, although the details of the patients' backgrounds were not mentioned, a recent review with regard to idiopathic

orbital inflammation including the 19 cases of myositis reported that eight of the nine patients who received RT experienced treatment failure.[8] Thus, we conclude that 20 Gy in 10 fractions of RT appears effective for palliating symptoms, however, long-term control is dismal for orbital myositis.

REFERENCES

1) Sergott RC, Glaser JS, Charyulu K. Radiotherapy for idiopathic inflammatory orbital pseudotumor. Indications and results. Arch Ophthalmol, 99: 853–856, 1981.
2) Slavin ML, Glaser JS. Idiopathic orbital myositis: report of six cases. Arch Ophthalmol, 100: 1261–1265, 1982.
3) Weinstein GS, Dresner SC, Slamovits TL, Kennerdell JS. Acute and subacute orbital myositis. Am J Ophthalmol, 96: 209–217, 1983.
4) Sekhar GC, Mandal AK, Vyas P. Non specific orbital inflammatory disease. Doc Ophthalmol, 84: 155–170, 1993.
5) Bessant DA, Lee JP. Management of strabismus due to orbital myositis. Eye, 9: 558–563, 1995.
6) Mannor GE, Rose GE, Moseley IF, Wright JE. Outcome of orbital myositis. Clinical features associated with recurrence. Ophthalmology, 104: 409–414, 1997.
7) Mombaerts I, Koornneef L. Current status in the treatment of orbital myositis. Ophthalmology, 104 :402–408, 1997.
8) Yuen SJ, Rubin PA. Idiopathic orbital inflammation: distribution, clinical features, and treatment outcome. Arch Ophthalmol, 121: 491–499, 2003.

Warthin Tumor of the Parotid Gland: Diagnostic Value of MR Imaging with Histopathologic Correlation

Mitsuaki Ikeda, Ken Motoori, Toyoyuki Hanazawa, Yuichiro Nagai, Seiji Yamamoto, Takuya Ueda, Hiroyuki Funatsu, and Hisao Ito

BACKGROUND AND PURPOSE: The purpose of our study was to describe the MR imaging appearance of Warthin tumors multiple MR imaging techniques and to interpret the difference in appearance from that of malignant parotid tumors.

METHODS: T1-weighted, T2-weighted, short inversion time inversion recovery, diffusion-weighted, and contrast-enhanced dynamic MR images of 19 Warthin tumors and 17 malignant parotid tumors were reviewed. MR imaging results were compared with those of pathologic analysis.

RESULTS: Epithelial stromata and lymphoid tissue with slitlike small cysts in Warthin tumors showed early enhancement and a high washout rate ($\geq$30%) on dynamic contrast-enhanced images, and accumulations of complicated cysts showed early enhancement and a low washout ratio (<30%). The areas containing complicated cysts showed high signal intensity on T1-weighted images, whereas some foci in those areas showed low signal intensity on short tau inversion recovery images. The mean minimum signal intensity ratios (SIR_{min}) of Warthin tumor on short tau inversion recovery (0.29 $\pm$ 0.22 SD) (P < .01) and T2-weighted images (0.28 $\pm$ 0.09) (P < .05) were significantly lower than those of malignant parotid tumors (0.53 $\pm$ 0.19, 0.48 $\pm$ 0.19). The average washout ratio of Warthin tumors (44.0 $\pm$ 20.4%) was higher than that of malignant parotid tumors (11.9 $\pm$ 11.6%). The mean apparent diffusion coefficient of Warthin tumors (0.96 $\pm$ 0.13 $\times$ $10^{-3}mm^2/s$) was significantly lower (P < .01) than that of malignant tumors (1.19 $\pm$ 0.19 $\times$ $10^{-3}mm^2/s$).

CONCLUSION: Detecting hypointense areas of short tau inversion recovery and T2-weighted images or low apparent diffusion coefficient values on diffusion-weighted images was useful for predicting whether salivary gland tumors were Warthin tumors. The findings of the dynamic contrast-enhanced study also were useful.

Imaging of the salivary glands has two purposes: first, to establish the precise extent and site of a salivary lesion, and second, to provide some indication of its pathologic nature. It is of major importance to determine whether a salivary gland tumor is benign or malignant and to assess its extent and relationship to adjacent structures preoperatively, because this information will strongly influence the choice of surgical procedure. Local excision or superficial parotidectomy is performed for benign tumors, whereas total

parotidectomy, with or without facial nerve removal, is performed for malignant tumors (1, 2). The pathologic diagnosis is typically determined by fine needle aspiration cytology. Although fine needle aspiration cytology is the most cost-effective and minimally invasive way to determine the histologic character of a parotid tumor, fine needle aspiration cytology is not always conclusive because specimen material from a small or deep mass may be insufficient (3–5). Thus, although there seems to be an important role for preoperative imaging, in reality its clinical significance is relatively little.

General agreement exists that the use of standard MR imaging sequences usually will not allow differentiation between parotid tumors (6–11). A few articles have reported the usefulness of dynamic contrast-enhanced and diffusion-weighted images for predicting whether salivary gland tumors are benign or malignant (12). This is complicated in that Warthin tumor,

TABLE 1: Histopathology diagnoses of salivary gland tumors

Diagnosis	No. of Lesions
Benign (n = 19)	
Warthin tumor	19
Malignant (n = 17)	
Mucoepidermoid carcinoma	1
Acinic cell adenocarcinoma	4
Adenoid cystic carcinoma	2
Salivary duct carcinoma	5
Squamous cell carcinoma	1
Basal cell adenocarcinoma	1
Carcinoma ex pleomorphic adenoma	3

a benign parotid gland tumor, is reported to mimic malignant neoplasm (13). MR imaging is an established and useful way of showing the morphology and extent of head and neck tumors and their relationship to adjacent structures. If, however, MR imaging could make a reliable distinction between benign and malignant neoplasms, its role and importance in diagnostics would become considerably more valuable. The purpose of this study, then, was to more precisely reveal the MR imaging features of Warthin tumor, which is described as a mimicker of malignant neoplasm, by using multiple MR images—T1-weighted, T2-weighted, short inversion time inversion recovery (STIR), diffusion-weighted, and dynamic contrast-enhanced MR images—to help ensure a correct diagnosis and differentiate the tumor from parotid malignancies.

Methods

Patients

Between November 2001 and January 2003, MR imaging studies of clinically suspected parotid tumors were performed before surgery or fine needle aspiration cytology. From this period, we reviewed the MR images of all pathologically proved Warthin tumors (19 tumors in 17 patients; 16 men and one woman; mean age, 65 years; age range, 46–85 years). Of the 17 patients with 19 tumors, nine with 11 lesions had undergone surgery, and eight with eight lesions had undergone needle biopsy. We also reviewed the MR imaging studies of all pathologically proved malignant parotid tumors (17 tumors in 17 patients; seven men and 10 women; mean age, 54 years; age range, 20–89 years). The distributions of Warthin tumors and malignant tumors are shown in Table 1.

MR Imaging Techniques

All MR imaging examinations were performed by using a 1.5-T MR imaging unit (GE Medical Systems, Milwaukee, WI) with a neurovascular array coil. T1-weighted images (400–500/9–14 [TR/TE]) of the transverse plane, STIR images (4000/30; echo train length, 12; inversion time, 150 ms) of the same transverse plane as the T1-weighted images, diffusion-weighted images (spin-echo single shot echo-planar sequence with b factors of 0 and 1000 s/mm^2) of the same transverse plane, and T2-weighted spin-echo images (4000/104; echo train length, 16) of the same transverse or coronal plane were obtained at a section thickness of 6 mm, an intersection gap of 1 mm, an acquisition matrix of 256 × 256 (128 × 128 on the diffusion-weighted images), and a field of view of 22 × 22 cm.

Dynamic contrast-enhanced MR images were obtained by 3D fat suppression T1-weighted multiphase spoiled gradient recalled imaging (6.3/1.4) for 4 minutes, with each phase lasting 27 seconds and then a 3-second interval, an effective section thickness of 4 mm, a field of view of 22 × 22 cm, and an acquisition matrix of 256 × 224. After the first set was obtained, contrast material injection was started immediately. Gadodiamide hydrate (Omniscan; Daiichi Pharmaceutical Corporation, Tokyo, Japan) was administered (0.2 mL/kg body weight) at a rate of 2.0 mL/s and then a 20-mL saline flush was delivered into the antecubital vein. Seven sets of dynamic contrast-enhanced images were obtained serially at 3, 33, 63, 93, 123, 153, and 183 seconds. Soon after the dynamic contrast-enhanced MR imaging, fat suppression T1-weighted images (340–400/20) of the same transverse plane as that of the unenhanced T1-weighted images or the coronal plane were obtained with an acquisition matrix of 256 × 224. Apparent diffusion coefficient (ADC) maps were automatically constructed from diffusion-weighted images. T1-weighted, dynamic contrast-enhanced, diffusion-weighted, and fat suppression contrast-enhanced T1-weighted images were obtained from all 19 Warthin tumors and 17 malignant tumors. Short tau inversion recovery images were obtained of all cases of Warthin tumors and 16 of 17 cases of malignant tumors; T2-weighted images were obtained from nine of 19 and 10 of 17 cases. This extensive routine MR imaging study can be performed in approximately 15 minutes.

Image and Pathologic Analyses

Two experienced radiologists (K.M., T.U.) evaluated the T1-weighted, STIR, and T2-weighted images to determine size, location (superficial lobe or deep lobe), nature of margin (definition and lobulation), and signal intensity of the tumors. In the evaluation of T1-weighted, T2-weighted, and STIR, the maximum (SI_{max}), minimum (SI_{min}), and CSF (SI_{csf}) signal intensities of the tumors were obtained. SIR was calculated as follows:

$$SIR_{max} = SI_{max}/SI_{csf}, \ SIR_{min} = SI_{min}/SI_{csf}.$$

One radiologist (K.M.) measured the signal intensities of the lesions on each dynamic image with an electronic cursor to define the region of interest in each patient. Where markedly heterogeneous enhancement was seen, multiple regions of interest were obtained. Time–signal intensity curves were then plotted from signal intensity values obtained for the tumors, the ipsilateral artery, and the ipsilateral vein. Time–signal intensity curves were divided into five types according to those presented by Takashima et al (14): type A, curve peaks 3 to 30 seconds after administration of contrast material; type B, curve peaks at 33 to 60 seconds; type C, curve peaks at 63 to 180 seconds; type D, gradual upward slope; and type E, unenhanced. Type C was divided into four subtypes: C1, curve peaks at 63 to 90 seconds; C2, curve peaks at 93 to 120 seconds; C3, curve peaks at 123 to 150 seconds; and C4, curve peaks at 153 to 180 seconds. Washout ratio was calculated by a modified method of that presented by Yabuuchi et al (12) as follows:

$$[(SI_{max} - SI_{3.5min})/(SI_{max} - SI_{pre})] \times 100(\%),$$

where SI_{max} was the signal intensity at maximal contrast enhancement, $SI_{3.5 \ min}$ the signal intensity at 3.5 minutes after contrast material administration, and SI_{pre} the unenhanced ("precontrast") signal intensity.

The ADC values of the lesions were measured on each diffusion-weighted image with an electronic cursor to define the region of interest. In measuring the signal intensities, we avoided obvious cystic portions. The ADC values of the spinal cord on diffusion-weighted images also were measured to assess the validity of our method and to compare our findings with the results from those of previous investigations. The tumors were marked at the top during surgery. For MR images,

they were cut on an axial plane. An experienced radiologist (K.M.) and a pathologist (Y.N.) correlated the MR images and pathologic specimens.

Results

Size, Location, and Shape of Tumors

Seventeen patients presented with 19 Warthin tumors of the parotid gland. Two cases had bilateral tumors. The average maximal cross-sectional diameter was 2.4 cm (range, 0.8–5.0 cm). Eighteen Warthin tumors were located in the caudal portion of the parotid gland. All tumors showed well-defined margins on T1-weighted and T2-weighted images. Six tumors revealed unclear margins on STIR images, because their signal intensities were as low as those of the parotid glands. Fourteen Warthin tumors showed well-defined margins on fat suppression T1-weighted images, with the other five showing unclear margins, because they were enhanced as much as the parenchyma of the parotid glands did. The average maximal cross-sectional diameter of the 17 malignant parotid tumors was 3.3 cm (range, 1.0–4.7 cm). Six malignant tumors showed well-defined margins, and the other 11 showed partially unclear or invasive margins on all MR images.

Signal Intensities of Tumors

All Warthin tumors had low signal intensity for the salivary gland and isointensity compared with muscle on T1-weighted images. Although small high-signal-intensity spots or areas could be detected in 12 or 19 Warthin tumors, no significant difference was observed between Warthin tumors and malignant parotid tumors in SIR_{max} and SIR_{min} on T1-weighted images. On T2-weighted and STIR images, many Warthin tumors had low-signal-intensity foci. The mean SIR_{min} of Warthin tumors on STIR images (0.29 ± 0.22 SD) was significantly lower ($P < .01$) than that of malignant parotid tumors (0.53 ± 0.19). The mean SIR_{min} of Warthin tumors on T2-weighted images (0.28 ± 0.09) was also significantly lower ($P < .05$) than that of malignant parotid tumors (0.48 ± 0.19). No significant differences in SIR_{max} were seen on STIR and T2-weighted images between Warthin tumors and malignant parotid tumors.

Time–Contrast Enhancement Ratio and Washout Ratio of Tumors

The artery curve peaked at 3 to 30 seconds after the administration of contrast agent (type A). Strongest enhancement of the vein was at 33 to 60 seconds (type B). Seven (36.8%) of the 19 Warthin tumors had type A curves, and the other 12 (63.2%) had type B curves. One Warthin tumor with a type A curve also had a type E curve. Six Warthin tumors with type B curves had one or two additional types of curves: type C1 in one case, both types D and E in one case, and type E in four cases. The average washout ratio of all 19 Warthin tumors was 44.0% ± 20.4, that of the

TABLE 2: Time intensity curves of tumors as shown by dynamic MR imaging

Case No.	Curve Types							
	A	B	C1	C2	C3	C4	D	E
WA 1	+ (41–50)							+
WA 2		+ (39–50)						+
WA 3	+ (22–38)							
WA 4		+ (50–58)						+
WA 5		+ (3–54)						
WA 6	+ (45)							
WA 7	+ (39)							
WA 8	+ (40–52)							
WA 9	+ (97)							
WA10		+ (45)						
WA11		+ (52)						
WA12		+ (22–32)						
WA13		+ (50)	+ (29)					
WA14		+ (22–47)						+
WA15		+ (18)						+
WA16		+ (73–102)						
WA17		+ (45)					+ (0)	+
WA18	+ (46–61)							
WA19		+ (11–55)						
AC 1		+ (22)						
AC 2		+ (25)						
AC 3		+ (20)						+
AC 4	+ (18–24)			+ (4.4)				
ME 1	+ (38)		+ (11)					
ACC1		+ (15)					+ (0)	
ACC2		+ (17)					+ (0)	+
SD 1			+ (11)	+ (6)				+
SD 2							+ (0)	
SD 3		+ (12)						+
SD 4							+ (0)	
SD 5	+ (16–27)						+ (0)	
SQ 1		+ (18–35)						
BC 1		+ (16)			+ (5)		+ (0)	
CEP1							+ (0)	
CEP2			+ (6)				+ (0)	+
CEP3		+ (25)	+ (4)					+

Note.—WA indicates Warthin tumor; AC, acinic cell adenocarcinoma; ME, mucoepidermoid carcinoma; ACC, adenoid cystic carcinoma; SD, salivary duct carcinoma; SQ, squamous cell carcinoma; BC, basal cell adenocarcinoma; CEP, carcinoma ex pleomorphic adenoma. Washout ratio, shown in parentheses, is expressed as a percentage.

seven type A tumors was 47.4% ± 17.8, and that of the 12 type B tumors was 42.3% ± 22.1. One type A and six type B tumors had areas showing a washout ratio lower than 30%. Of the malignant parotid tumors, eight showed type D curves. The average value of the washout ratio of all 17 malignant parotid tumors was 11.9% ± 11.6. The time–signal intensity curves and washout ratios of the tumors are summarized in Table 2.

ADC Values of Tumors

All diffusion-weighted images of 19 Warthin tumors and 17 malignant tumors showed irregularly high signal intensities. The ADC values of both tumors and of spinal cord were measured. The average of the ADC values of the 19 Warthin tumors (0.96 ±

0.13, 0.72 to 1.17×10^{-3} mm^2/s) was significantly lower ($P < .01$) than that of the 17 malignant tumors (1.19 ± 0.19, 0.79 to 1.65×10^{-3} mm^2/s). The average of the ADC values of the Warthin tumors was also lower than that of the spinal cord (1.02 ± 0.05, 0.93 to 1.16×10^{-3} mm^2/s), but not significantly.

Correlations between Radiologic and Pathologic Findings

All dissected Warthin tumors had fibrous capsules at the maximal diameter section. The fibrous capsules, sometimes shown on MR images, varied in thickness, and the tumors were separated from normal major glands. The high-signal-intensity foci on unenhanced STIR and T2-weighted images corresponded to cysts (Fig 1). These macroscopic cysts usually were sizable, and they lost their contents when the tumors were subjected to specimen preparation. They showed high ADC values ($1.63 \pm 0.50 \times 10^{-3}$ mm^2/s) on diffusion-weighted images. Microscopic cysts in the macroscopic solid components of Warthin tumors varied from small slitlike spaces to those several centimeters in length and occupied a considerable portion of the entire lesion. The microscopic slitlike cysts, mostly not detectable as high-signal-intensity foci on STIR and T2-weighted images, showed characteristic low ADC values on diffusion-weighted images. They were filled with proteinous secretion (Fig 1). High-signal-intensity areas on T1-weighted images corresponded to areas with accumulations of microscopic cysts containing proteinous fluid with foamy cells, red cells, and neutrophils (Fig 2). Sometimes, the macroscopic solid area with these microscopic complicated cysts showed characteristic low signal intensities on STIR images. The typical components of Warthin tumor (slitlike cysts, or arborescent spaces lined by a papillary proliferation of bilayered oncocytic epithelia with supporting stroma composed largely of lymphoid tissue) showed type A or B perfusion curves with high washout ratio ($\geq 30\%$) on dynamic contrast-enhanced images and low ADC values ($0.88 \pm 0.17 \times 10^{-3}$ mm^2/s) on diffusion-weighted images (Fig 1). The epithelial stroma and lymphoid tissue with accumulating microscopic complicated cysts also showed type A or B time–signal intensity curves on dynamic images, but their washout ratio was sometimes low ($<30\%$) (Fig 2).

Discussion

It is clinically important to determine preoperatively whether a salivary gland tumor is benign or malignant, because such a determination will strongly influence the choice of surgical procedure. If the tumor is benign, waiting to remove it allows it to grow larger, making the eventual surgery more difficult and prone to complications. In case of pleomorphic adenoma, prolonged delay can lead to malignant change, and therefore prompt local excision or superficial parotidectomy. If the mass is initially malignant, total

parotidectomy with or without facial nerve removal is performed without delay (1, 2). As for Warthin tumors, enucleation is recommended when the diagnosis is known preoperatively, and $<2\%$ recurrence is reported (15–17).

The morphology and extent of head and neck tumors and their relationship to adjacent structures can be clearly shown by MR imaging. However, it is commonly thought that MR imaging cannot make a reliable distinction between benign and malignant neoplasms, and that a pathologic diagnosis by such method is out of reach (6–11). Nevertheless, Yabuuchi et al (12) and Wang et al (13) have reported that dynamic contrast-enhanced and diffusion-weighted imaging methods are useful for predicting whether salivary gland tumors are benign or malignant.

Warthin tumor generally has been regarded as the second most common benign tumor of the parotid gland after pleomorphic adenoma. It occurs largely in middle-aged and older men (18) and usually in the parotid gland or periparotid region, mostly involving the inferior pole of the gland. Multicentric occurrence is seen more often with Warthin tumor than any other salivary gland tumor. Warthin tumors usually are spherical to ovoid, have a smooth surface, and normally are 2 to 4 cm in diameter. All tumors in this study showed well-defined margins on T1- and T2-weighted images, and the average maximal cross-sectional diameter of the Warthin tumors at our institute was 2.4 cm (range, 0.8–5.0 cm). Our data agreed well with data reported in previous articles (18, 19).

Warthin tumor is an adenoma with a variable number of cysts filled with mucoid or brown fluid. The cysts are lined with papillary proliferations of bilayered oncocytic epithelia and supporting stroma composed of great amounts of follicle-containing lymphoid tissue. The tumor occasionally contains focal hemorrhage and necrosis. In our study, some large cysts could be detected as high-signal-intensity foci on STIR and T2-weighted images, but small slitlike cysts were not detected. The areas including complicated cysts containing proteinous fluid with foamy cells, red cells, and neutrophils showed high signal intensity on T1-weighted images. Minami et al (20) reported that cysts containing cholesterol crystals appeared on T1-weighted images as high-signal-intensity areas. In the present study, cysts containing cholesterol crystals could not be detected, but some large cysts leaked fluid when the tumor was cut. Some areas of the high-signal-intensity lesions on T1-weighted images showed characteristic low signal intensity on STIR images. STIR is sensitive to changes in T1 and T2 values, and an inversion time was chosen so that the signal intensity of fat was zero at the time of 90 pulses. T1 values of hemorrhagic lesions change depending on the time from the start of hemorrhaging, so some hemorrhagic lesions with the same T1 value as fat might show hypointensity on STIR images (21, 22). However, this hypothesis could not completely explain the signal intensities of STIR, as the marked low-signal-intensity foci on STIR images do not al-
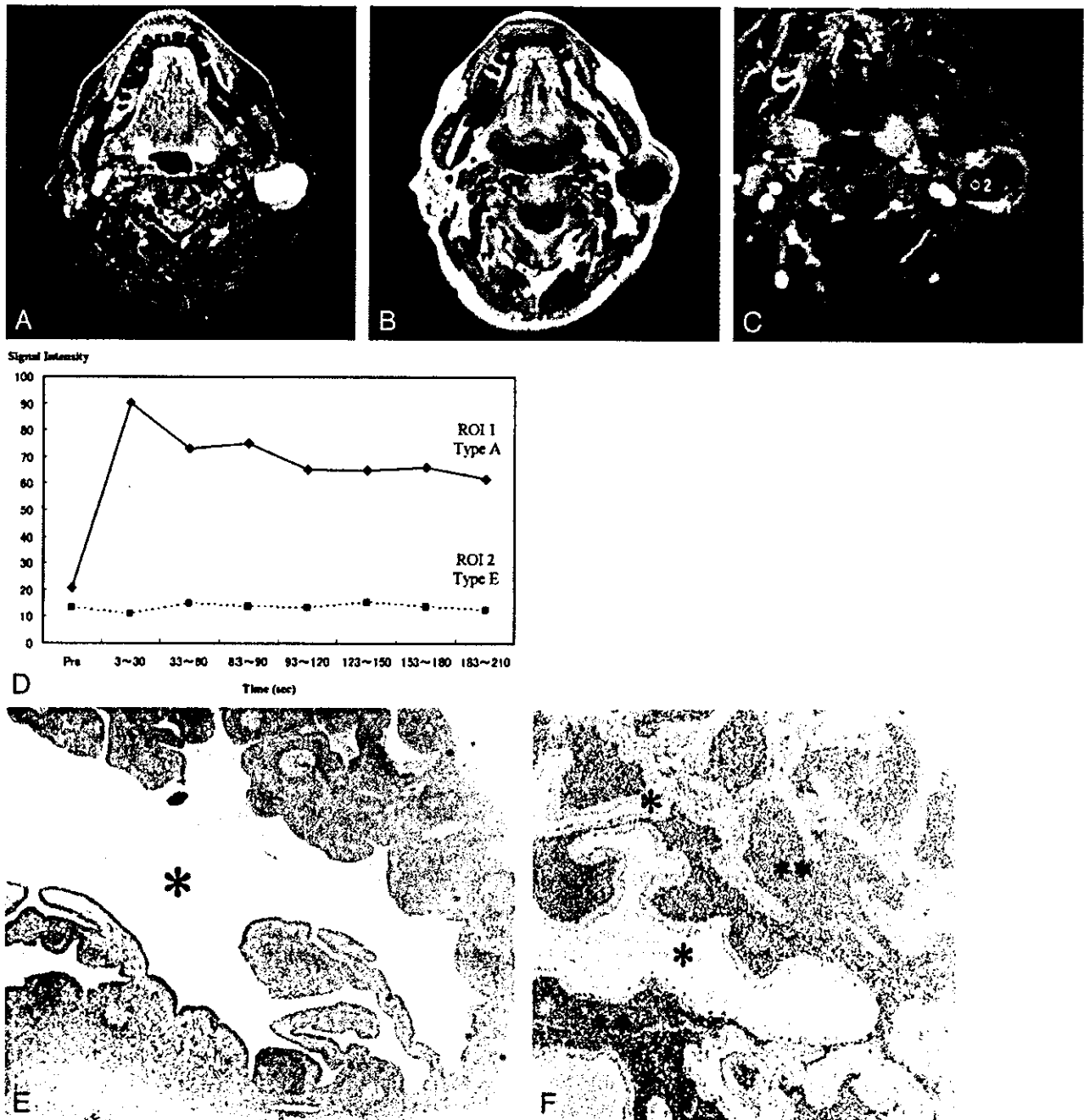
FIG 1.   Images of a Warthin tumor in the left parotid gland of a 70-year-old man.

A, STIR image (4000/30), obtained in the axial plane, shows the tumor with moderate-to-high signal intensity. The high-signal-intensity area is a cystic lesion (*); the area showed no enhancement on contrast-enhanced images (see panel *C*, region of interest 2).

B, T1-weighted image (400/9), obtained in the axial plane, shows a hypointense tumor.

C, Fat suppression contrast-enhanced T1-weighted image (300/20), obtained in the coronal plane, shows solid (region of interest 1) and cystic (region of interest 2) tumor in the inferior pole of the parotid gland.

D, Signal intensity graph shows that the washout ratio of the solid component was 41%. The cystic region shows no enhancement (type E). The ADC values of the solid and cystic components were 0.96×10^{-3} mm^2/s and 2.74×10^{-3} mm^2/s, respectively. The ADC value of the spinal cord was 1.02×10^{-3} mm^2/s.

E, Axial section of the specimen shows solid and large cystic components (*). The large cyst lost its contents.

F, Solid component has slitlike or dendriform spaces (*) lined with papillary proliferation of bilayered oncocytic epithelia, with supporting stroma composed largely of lymphoid tissue (**). The small slitlike cysts are filled with proteinous secretion.

ways appear as high-signal-intensity areas on T1-weighted images.

Both the cellular matrix with usual large cysts and with complicated cysts, which were small and slitlike, showed type A or B time–signal intensity curves on

dynamic contrast-enhanced images. Our data agreed well with data reported in previous articles (8, 12, 14). According to Yabuuchi et al (12), a correlation existed between the washout ratio and cellularity-stromal grade; they reported that Warthin tumors with
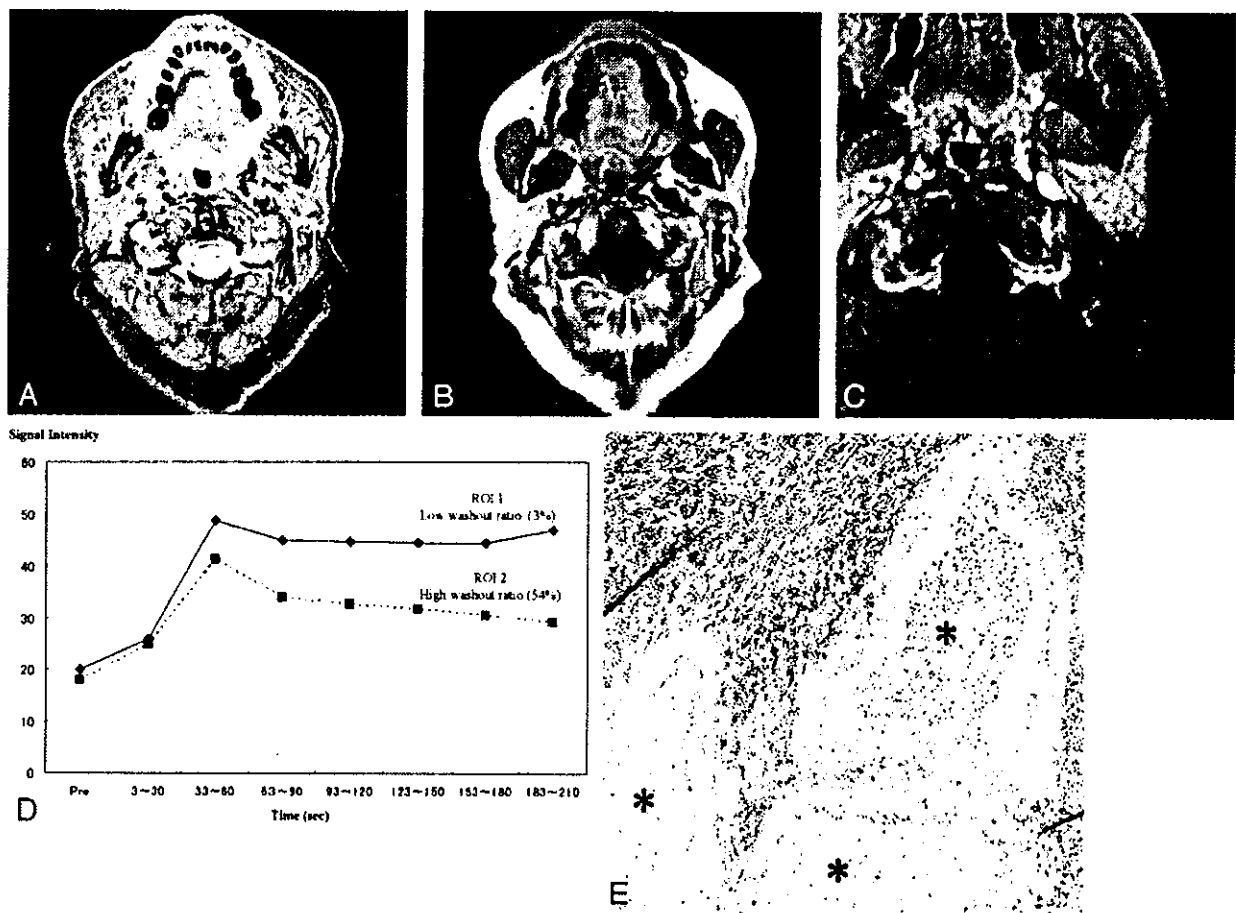
Fig 2.   Images of a Warthin tumor in the left parotid gland of a 61-year-old man.

A, STIR image (4000/30), obtained in the axial plane, shows the tumor to be iso- to hypointense to the parotid gland. Characteristically small low-signal-intensity foci (arrows) can be detected. The margin of the tumor also has hypointense foci.

B, T1-weighted image (400/9), obtained in the axial plane, shows the tumor to have the isointensity of muscle and relatively high-signal-intensity areas, whereas the STIR image shows low-signal-intensity areas (arrows). The margin of the tumor also is hypointense on T1-weighted images.

C, Axial dynamic contrast-enhanced image shows all areas of this tumor to have type B perfusion curves.

D, Signal intensity graph shows that foci that showed hypointensity on the STIR image and relatively high signal intensity on the T1-weighted image (region of interest 1) had a low washout ratio (3%) and the other region (region of interest 2) had a high washout ratio (54%).

E, Axial section of the specimen shows cysts containing proteinous fluid with inflammatory cells (*).

many microvessels and hypercellular stromata had a high washout ratio (≥30%) and that malignant tumors with many microvessels and hypocellular stromata had a low washout ratio (<30%). In our study, 12 (63%) of the 19 Warthin tumors showed an exclusively high washout ratio, except in the unenhanced areas. The other seven (37%) had low washout ratio components, and one of the seven had low washout ratio components only. In the present study, a difference was shown concerning washout ratio between the areas containing usual microscopic cysts and microscopic complicated cysts. The permeability and diffusion of contrast material in the two areas can be assumed to be different, with contrast material possibly diffusing in complicated cysts as it does in foamy cells, red cells, and neutrophils. Complicated cysts would then form an extracellular matrix containing slowly distributed and accumulating contrast material.

The average value of the washout ratio of all 19 Warthin tumors was 44.0% ± 20.4 and that of all 17

malignant parotid tumors was 11.9% ± 11.6. A 30% washout ratio is generally considered the borderline for predicting whether salivary gland tumors are benign or malignant.

The average ADC value of 19 Warthin tumors ($0.96 \pm 0.13 \times 10^{-3}$ mm²/s) was significantly lower than that of 17 malignant tumors ($1.19 \pm 0.19 \times 10^{-3}$ mm²/s) ($P < .01$). Macroscopic cysts showing high signal intensity on STIR and T2-weighted images had high ADC values. In the case of Warthin tumors, epithelial and lymphoid stromata with microscopic slitlike cysts filled with proteinous fluid had low ADC values. It was not surprising that the mean ADC value of large cystic components was markedly higher than that of hypercellular tissue, because the mobility of water protons is relatively freer in fluid than in other tissues. The small cysts filled with proteinous fluid in Warthin tumors could not be detected as high-signal-intensity foci on STIR and T2-weighted images, and they had lower ADC values than the high-signal-

intensity cysts on STIR and T2-weighted images. The difference between the two types of cysts can be attributed to the viscosity of their contents. Highly viscosous contents, such as dense proteinous secretions, show lower ADC values than those of serous fluid (23). Hypercellular matrix and microscopic slit-like cysts filled with highly viscosous contents in Warthin tumor have low ADC values on diffusion-weighted images. According to Wang et al (13), the mean ADC value of malignant lymphomas ($0.66 \pm 0.17 \times 10^{-3}$ mm^2/s) was significantly smaller ($P < .001$) than that of carcinomas ($1.13 \pm 0.43 \times 10^{-3}$ mm^2/s), which in turn was significantly smaller ($P = .002$) than that of benign solid tumors. They used an ADC value smaller than 1.22×10^{-3} mm^2/s for predicting malignancy. Their study included only three Warthin tumors among 10 benign solid tumors of the head and neck. The ADC values of spinal cords in our study were similar to those reported by Wang et al, but all Warthin tumors in our study would be falsely positive if the criterion presented by Wang et al were used. We think that a low ADC value is a noteworthy feature of Warthin tumor.

Conclusion

Most Warthin tumors were revealed to involve the inferior pole of parotid glands and to have a smooth margin on T1- and T2-weighted images. Warthin tumor, epithelial stroma, and lymphoid tissue with microscopic cysts filled with proteinous secretion showed early enhancement, type A or B perfusion curves, and a high washout ratio ($\geq30\%$) on dynamic contrast-enhanced images and a low ADC value on diffusion-weighted images. The cellular components with accumulated microscopic cysts containing proteinous fluid with foamy cells, red cells, and neutrophils were recognized as high-signal-intensity foci on T1-weighted images and characteristically hypointense areas on STIR and T2-weighted images. These cellular components with accumulated microscopic complicated cysts showed a low washout ratio ($<30\%$) on dynamic contrast-enhanced images. The additional information of ADC, washout ratio, and time–signal intensity curves confirmed that the tumor was a Warthin tumor. A 30% washout ratio threshold tended to be useful for predicting whether salivary gland tumors were benign or malignant. The ADC values of Warthin tumors ($0.96 \pm 0.13 \times 10^{-3}$ mm^2/s) were significantly lower ($P < .01$) than those of malignant tumors ($1.19 \pm 0.19 \times 10^{-3}$ mm^2/s), as were the signal intensities of the characteristic hypointense areas of Warthin tumors on STIR and T2-weighted images. Our extensive routine MR imaging study requires approximately 15 minutes to obtain all images and is excellent not only for assessing the extent of a salivary gland tumor and the relationship to adjacent structures, but also for determining whether the tumor is benign or malignant.

References

1. Donovan DT, Conley JJ. Capsular significance in parotid tumor surgery: reality and myths of lateral lobectomy. *Laryngoscope* 1984;94:324–329
2. Dykun RJ, Deitel M, Borowy ZJ, Jackson S. Treatment of parotid neoplasms. *Can J Surg* 1980;23:14–19
3. Que Hee CG, Perry CF. Fine-needle aspiration cytology of parotid tumours: Is it useful? *Aust N Z J Surg* 2001;71:345–348
4. Zbaren P, Schar C, Hotz MA, Loosli H. Value of fine-needle aspiration cytology of parotid gland masses. *Laryngoscope* 2001;111:1989–1992
5. Flezar M, Pogacnik A. Warthin's tumour: unusual vs. common morphological findings in fine needle aspiration biopsies. *Cytopathology* 2002;13:232–241
6. Schlakman BN, Yousem DM. MR of intraparotid masses. *AJNR Am J Neuroradiol* 1993;14:1173–1180
7. Joe VQ, Westesson PL. Tumors of the parotid gland: MR imaging characteristics of various histologic types. *AJR Am J Roentgenol* 1994;163:433–438
8. Tsushima Y, Matsumoto M, Endo K, Aihara T, Nakajima T. Characteristic bright signal of parotid pleomorphic adenomas on T2-weighted MR images with pathological correlation. *Clin Radiol* 1994;49:485–489
9. Vogl TJ, Dresel SH, Spath M, et al. Parotid gland: plain and gadolinium-enhanced MR imaging. *Radiology* 1990;177:667–674
10. Freling NJ, Molenaar WM, Vermey A, et al. Malignant parotid tumors: clinical use of MR imaging and histologic correlation. *Radiology* 1992;185:691–696
11. Browne RF, Golding SJ, Watt-Smith SR. The role of MRI in facial swelling due to presumed salivary gland disease. *Br J Radiol* 2001;74:127–133
12. Yabuuchi H, Fukuya T, Tajima T, Hachitanda Y, Tomita K, Koga M. Salivary gland tumors: diagnostic value of gadolinium-enhanced dynamic MR imaging with histopathologic correlation. *Radiology* 2003;226:345–354
13. Wang J, Takashima S, Takayama F, et al. Head and neck lesions: characterization with diffusion-weighted echo-planar MR imaging. *Radiology* 2001;220:621–630
14. Takashima S, Noguchi Y, Okumura T, Aruga H, Kobayashi T. Dynamic MR imaging in the head and neck. *Radiology* 1993;189:813–821
15. Ebbs SR, Webb AJ. Adenolymphoma of the parotid: aetiology, diagnosis and treatment. *Br J Surg* 1986;73:627–630
16. Heller KS, Attie JN. Treatment of Warthin's tumor by enucleation. *Am J Surg* 1988;156:294–296
17. Batori M, Mariotta G, Giovannone G, Casella G, Casella MC. Warthin's tumor of parotid gland: treatment of a retroneural lesion by enucleation. *Eur Rev Med Pharmacol Sci* 2002;6:105–111
18. Eveson JW, Cawson RA. Salivary gland tumours: a review of 2410 cases with particular reference to histological types, site, age and sex distribution. *J Pathol* 1985;146:51–58
19. Ellis GL, Auclair PL. Warthin's tumor (papillary cystadenoma lymphomatosum). In: *Tumors of the Salivary Glands: Atlas of Tumor Pathology*. Washington, D.C.: Armed Forces Institute of Pathology; 1996:68–80
20. Minami M, Tanioka H, Oyama K, et al. Warthin tumor of the parotid gland: MR-pathologic correlation. *AJNR Am J Neuroradiol* 1993;14:209–214
21. Chaudhuri R, Bingham JB, Crossman JE, Gleeson MJ. Magnetic resonance imaging of the parotid gland using the STIR sequence. *Clin Otolaryngol* 1992;17:211–217
22. Ryu KN, Jin W, Ko YT, et al. Bone bruises: MR characteristics and histological correlation in the young pig. *Clin Imaging* 2000;24:371–380
23. Garcia-Perez AI, Lopez-Beltran EA, Kluner P, Luque J, Ballesteros P, Cerdan S. Molecular crowding and viscosity as determinants of translational diffusion of metabolites in subcellular organelles. *Arch Biochem Biophys* 1999;362:329–338

Inter- and Intratumoral Variability in Magnetic Resonance Imaging of Pleomorphic Adenoma

An Attempt To Interpret the Variable Magnetic Resonance Findings

Ken Motoori, MD, Seiji Yamamoto, MD, Takuya Ueda, MD, Koichi Nakano, MD, Takayuki Muto, MD, Yuichiro Nagai, MD, Mitsuaki Ikeda, MD, Hiroyuki Funatsu, MD, and Hisao Ito, MD

Objectives: The purpose of our study was to describe the various magnetic resonance (MR) findings of pleomorphic adenoma and to interpret these findings.

Methods: MR studies of 33 pleomorphic adenomas and 13 malignant tumors in the major salivary glands were reviewed.

Results: High signal intensity on short-inversion-time inversion recovery (STIR) and T2-weighted (T2W) images, progressive enhancement on dynamic MR images, and high apparent diffusion coefficient (ADC) values on diffusion-weighted (DW) images reflected myxoid-dominant components in pleomorphic adenomas. Hypercellularity with less-myxoid stroma showed reduced signal intensity on STIR and T2W images and also reduced ADC values on DW images, and the peak of time versus signal intensity curves (TICs) was reached earlier on dynamic MR images.

Conclusions: The MR images of hypercellularity components in pleomorphic adenoma overlap with those of malignant parotid tumors. Detecting myxoid components by STIR, T2W, DW, and dynamic MR images is useful for predicting whether salivary gland tumors are pleomorphic adenoma or not.

Key Words: magnetic resonance (MR) imaging, parotid gland, pleomorphic adenoma

(*J Comput Assist Tomogr* 2004;28:233–246)

P leomorphic adenoma, the most common tumor of salivary glands, can successfully be treated by surgery if the capsule is completely removed. There is agreement that enucleation of the pleomorphic adenoma of the salivary gland, defined as opening the capsule of the tumor followed by surgical removal or aspiration of its contents, leads to a high recurrence rate.[1-4] Similarly, surgical exposure of the tumor or the tumor capsule, including needle biopsy and fine-needle aspiration cytology (FNAC), risks spillage and dramatically increases the risk of recurrence,[1-4] and the soft tissue penetrated by the needle would require resection together with the tumor. Therefore, preoperative diagnosis without the use of biopsy would certainly be advantageous for finally facilitating optimal results from surgery. Pleomorphic adenoma is renowned for its cytomorphological and architectural variability. Despite their protean histopathology, all tumors share the essential diagnostic features of being composed of both epithelial (cellular) and mesenchymal-like (myxoid) tissues. The proportions of these components vary widely, and one or the other is often predominant. Thus, it can be supposed that pleomorphic adenoma will show a variety of imagings. Although many reports have been published on the magnetic resonance (MR) imaging of pleomorphic adenoma with respect to the histologic specificity of signal characteristics,[5-10] time versus signal intensity curves (TICs) on dynamic MR images,[11-13] and apparent diffusion coefficients (ADCs) calculated from diffusion-weighted MR images,[14] the variability of MR findings of pleomorphic adenoma have not extensively been studied. The purpose of this study is to more precisely reveal the MR features of pleomorphic adenoma using multiple MR sequences, T1-weighted, T2-weighted, short-inversion-time inversion recovery, diffusion-weighted images, and dynamic contrast-enhanced MR images to help ensure a correct diagnosis and differentiate the tumor from other parotid malignancy.

PATIENTS AND METHODS

Patients

We reviewed MR studies of 33 pathologically proven pleomorphic adenomas in 33 patients, 9 men and 24 women, with a mean age of 50 years (15–70 years). Of these, 30 lesions were in the parotid glands and 3 lesions were in the submandibular glands. We also reviewed MR studies of 13 pathologically proven malignant parotid tumors in 13 patients, 5 men

and 8 women, with a mean age of 50 years (20–83 years). The distribution of pleomorphic adenomas and malignant tumors are shown in Table 1.

MR Imaging Techniques

All MR examinations were performed using 1.5-T MR units (GE Medical Systems, Milwaukee, WI) with a neurovascular array coil. T1-weighted (T1W) images [400-500/9-14 (repetition time ms/echo time ms)] of the transverse plane, short-inversion-time inversion recovery (STIR) images [4000/30, 12 (echo train length), 150 (inversion time ms)] of the same transverse plane to T1W images, diffusion-weighted (DW) images (spin-echo single-shot echo-planar sequence with b factors of 0 and 1,000 s/mm^2) of the same transverse plane, and T2-weighted (T2W) SE images [4000/104, 16 (echo train length)] of the same transverse or coronal plane were obtained at a section thickness of 6 mm, an intersection gap of 1 mm, an acquisition matrix of 256 × 256 (128 × 128 on DW images), and a field of view (FOV) of 22 × 22 cm. Dynamic contrast-enhanced MR images were obtained by 3-dimensional fat suppression T1W multiphase spoiled gradient-recalled-echo (SPGR) [6.3/1.4 (repetition time ms/echo time ms)] for 4 minutes, with each phase lasting 27 seconds followed by a 3-second interval, an effective section thickness of 4 mm, a FOV 22 × 22 cm, and an acquisition matrix of 256 × 224. After the first set was obtained, contrast material injection was started immediately. Gadodiamide hydrate (Omniscan, Daiichi Pharmaceutical Corporation, Tokyo, Japan) was administered (0.2 mL/kg body weight) at a rate of 2.0 mL/s followed by a 20-mL saline flush into the antecubital vein. Seven sets of dynamic contrast-enhanced images were obtained serially at 3, 33, 63, 93, 123, 153, and 183 seconds. Soon after dynamic contrast-enhanced MR imaging, fat-suppression T1W images [340-400/20 (repetition time ms/echo time ms)] of the same transverse plane to precontrast-enhanced T1W images were obtained with an acquisition matrix of 256 × 224. ADC maps were automatically constructed from DW images. T1W images, gadolinium-enhanced dynamic images, and fat-suppression contrast-enhanced T1W images were obtained

TABLE 1. Histopathologic Diagnosis of Salivary Gland Tumors

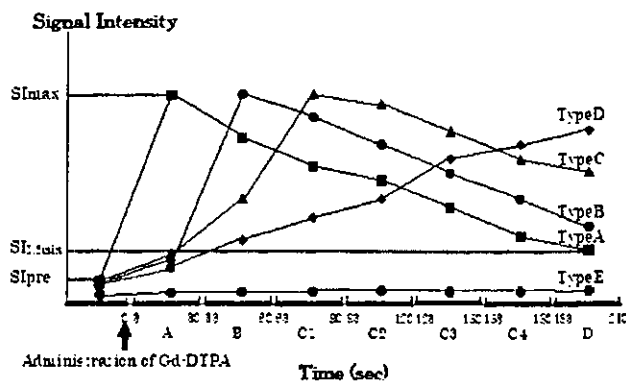| Diagnosis	No. of Lesions
Benign (*n* = 33)	
Pleomorphic adenoma	33
Malignant (*n* = 16)	
Mucoepidermoid carcinoma	1
Acinic cell adenocarcinoma	4
Adenoid cystic carcinoma	3
Salivary duct carcinoma	5
Malignant lymphoma	3

FIGURE 1. TICs of pleomorphic adenomas are plotted from signal intensity on dynamic MR images. TICs were divided into 5 types: type A, curve peaks 3–30 seconds after administration of contrast material; type B, curve peaks at 33–60 seconds; type C, curve peaks at 63–180 seconds; type D, gradual upward slope; and type E, nonenhanced. Type C was divided into 4 subtypes: C1, curve peaks at 63–90 seconds; C2, 93–120 seconds; C3, 123–150 seconds; and C4, 153–180 seconds. Washout ratio (WR), expressed as a percentage, was defined as follows: [(SI$_{max}$ − SI$_{3.5min}$) / (SI$_{max}$ − SI$_{pre}$)] × 100 (%).

from all 33 pleomorphic adenomas and 13 malignant tumors. STIR images were obtained from 28/33 cases of pleomorphic adenomas and 12/13 cases of malignant tumors, T2W images from 13/33 and 5/13 cases, and DW images from 22/33 and 13/13 cases, respectively.

Image and Pathologic Analyses

Two experienced radiologists (K.M., T.U.) evaluated the T1W, STIR, and T2W images to determine size, location (superficial lobe or deep lobe), nature of margin (definition and lobulation), and signal intensity of the tumors. In the evaluations of T2W images and STIR, maximum (SI$_{max}$) and minimum (SI$_{min}$) signal intensities of the tumors were used. Signal intensities of cerebral spinal fluid (CSF) (SI$_{csf}$) were also obtained. The signal intensity ratio (SIR) was calculated as follows:

$$SIR_{max} = SI_{max} / SI_{csf}, \quad SIR_{min} = SI_{min} / SI_{csf}.$$

One radiologist measured the signal intensities of the lesions on each dynamic image with an electronic cursor to define the region of interest (ROI) in each patient. Where markedly heterogeneous enhancement was seen, multiple ROIs were obtained. TICs were then plotted from signal intensity values obtained for the tumors, the ipsilateral artery, and the ipsilateral vein. TICs were divided into 5 types according to those of Takashima et al[11]: type A, curve peaks at 3–30 seconds after administration of contrast material; type B, curve peaks at 33–60 seconds; type C, curve peaks at 63–180 seconds; type D, gradual upward slope; and type E, nonenhanced. Type C was divided into 4 subtypes: C1, curve peaks at 63–90 seconds; C2, 93–120 seconds; C3, 123–150 seconds; and, C4,
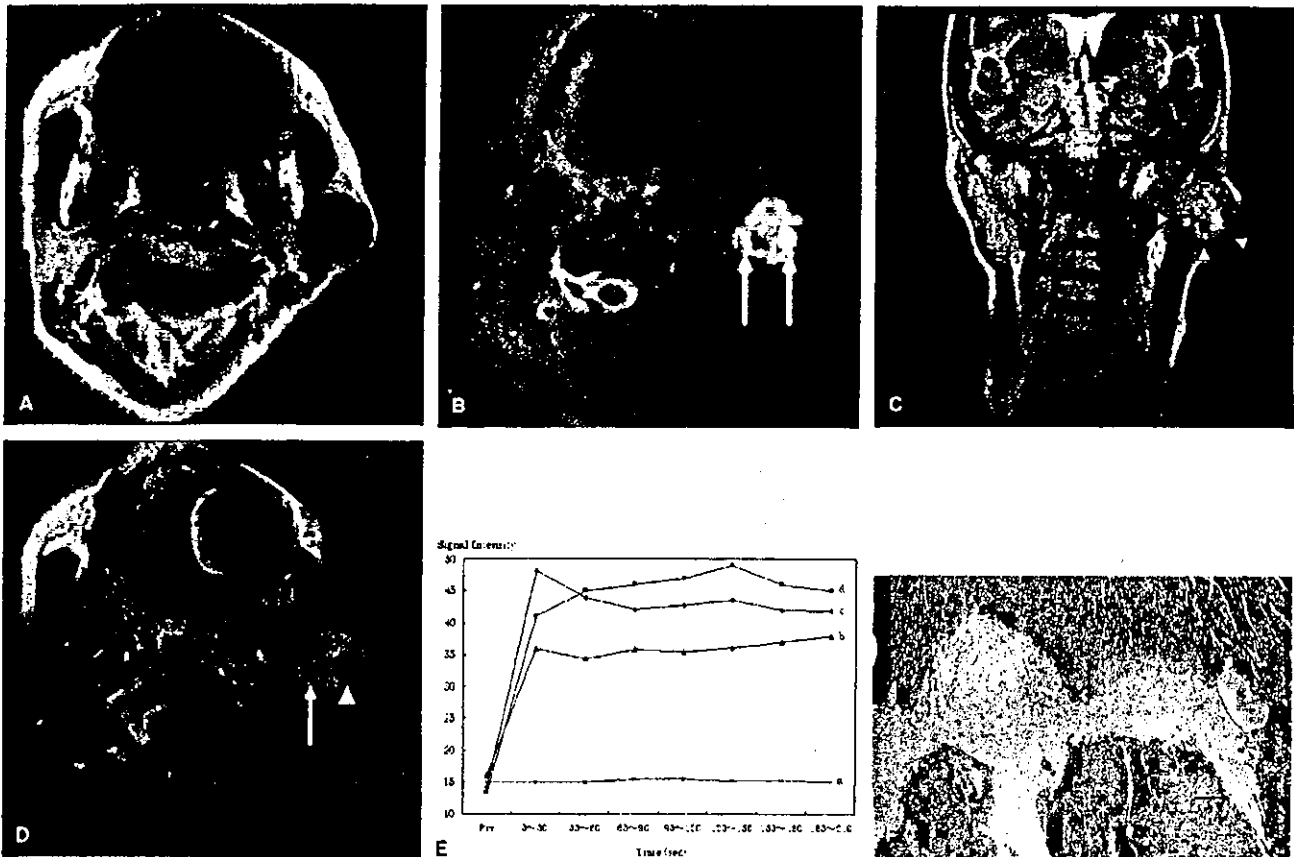
FIGURE 2. A, T1W image [400/9 (TR/TE), axial plane] of the maximal diameter section shows a lobulated tumor of isointensity for muscle in the superficial lobe of the left parotid gland. B, STIR image (4000/30, axial plane) shows moderately high-intensity tumor with 2 marked high-intensity regions (arrows). C, T2W image (4000/100, coronal plane) shows a lobulated tumor with hypointensity rim. This hypointensity rim (arrowheads) could not be detected on T1W and STIR images. D, Fat-suppression contrast-enhanced T1W image (340/20, axial plane) shows heterogeneous enhancement. The lateral region showing hyperintensity on STIR (arrowhead) is not enhanced, and the medial region (arrow) is slightly enhanced. The lateral focus is a cyst, and the medial region can be considered to be myxoid tissue. E, This tumor has 4 types of TICs on dynamic MR images: type A, C3, D, and E perfusion curves. a, The lateral region showing hyperintensity on STIR has nonenhancement. b, The medial hyperintensity region has type D perfusion curve. c and d, The other regions have type A and C3 perfusion curves. F, Maximal diameter axial section of the specimen shows that the peripheral region has not only abundant hypercellular components with capillary vessels (*) but also small slit-like or wedge-shaped fibromyxoid islands (arrows).

153–180 seconds. Washout ratio (WR) was calculated by modified method of Yabuuchi et al[13] as follows:

$$[(SI_{max} - SI_{3.5min}) / (SI_{max} - SI_{pre})] \times 100\ (\%),$$

where SI_{max} was the signal intensity at maximal contrast enhancement, $SI_{3.5min}$ the signal intensity at 3.5 minutes after contrast material administration, and SI_{pre} the precontrast signal intensity. The parameters of TIC are summarized in Fig. 1.

The ADC values of the lesions were measured on each DW image with an electronic cursor to define the ROI. Multiple ROIs were obtained when differing values were observed. Maximum and minimum ADC values of tumors were obtained. The ADC values of the spinal cord on DW images

were also measured to assess the validity of our method and to compare our findings with the results from previous investigations. The tumors were marked at the top during surgery. For MR images, they were cut on an axial plane. An experienced radiologist and a pathologist correlated the MR images and pathologic specimens.

RESULTS

Size, Location, and Shape of Pleomorphic Adenomas

The average maximal cross-sectional diameter of the 33 pleomorphic adenomas was 2.6 cm (1.0–5.8 cm). Fourteen ad-

enomas were located in the left superficial lobe of the parotid gland, 7 in the right superficial lobe, 6 in the left deep lobe, 3 in the right deep lobe, and 3 in the right submandibular gland. All pleomorphic adenomas showed well-defined margins. On T2W images, the low-intensity capsules, between high-intensity tumors and high-intensity parotid gland, were easily detected (Fig. 2). On the other hand, T1W and STIR images did not clearly reveal low-intensity capsules as did the T2W images. Twenty-three pleomorphic adenomas showed lobulations at the margins. The average maximal cross-sectional diameter of the 13 malignant parotid tumors was 3.2 cm (1.0–7.0 cm). Three malignant tumors showed well-defined margins, and the other 10 showed partially unclear or invasive margins.

Signal Intensities of Tumors

All tumors had low intensity for salivary gland and isointensity for muscle on T1W images. On T2W and STIR images, many pleomorphic adenomas had high intensity with multiple relatively low-intensity foci. The signal intensity patterns of 33 pleomorphic adenomas, 28 cases on STIR and 13 cases on T2W images, and 13 malignant parotid tumors, 12 cases on STIR and 5 cases on T2W images, are summarized in Figs. 3(A) and (B). The mean SIR_{max} of pleomorphic adenomas on STIR images was 1.06 ± 0.15 (SD), and characteristic bright signals with a higher intensity than that of CSF ($SIR \geq 1.0$) were seen in 20/28 (71.4%) tumors. The mean SIR_{max} of pleomorphic adenomas on STIR images was significantly ($P < 0.01$) higher than that of malignant parotid tumors $[0.81 \pm 0.21$ (SD)$]$. The mean SIR_{max} of pleomorphic adenomas on T2W images was 0.84 ± 0.21 (SD). Characteristic bright signals on T2W images were seen in 3/13 (23.1%) tumors. There was no significant difference between pleomorphic adenomas and malignant parotid tumors in SIR_{min} on STIR and in SIR_{max} and SIR_{min} on T2W images.

Time versus Signal Intensity Curves and Washout Ratio of Tumors

The artery curve peaked 3–30 seconds after administration of the contrast agent (type A). The vein was most enhanced at 33–60 seconds (type B). All pleomorphic adenomas showed type D perfusion curves, with 12 of them showing this type exclusively. The other 21 pleomorphic adenomas had regions that showed additional types of curves as well: type A in 2 cases, type B in 5 cases, type C1 in 1 case, type C2 in 4 cases, type C3 in 5 cases, type C4 in 10 cases, and type E in 2 cases. Four cases of malignant parotid tumors showed type D perfusion curves, with 2 of them showing this type exclusively, and the other 2 had regions that showed additional types of curves. washout ratio (WR) was calculated and summarized with patterns of perfusion curves in Table 2.

ADC Values of Tumors

All DW images of 22 pleomorphic adenomas and 13 malignant tumors showed irregular high intensities. The maxi-
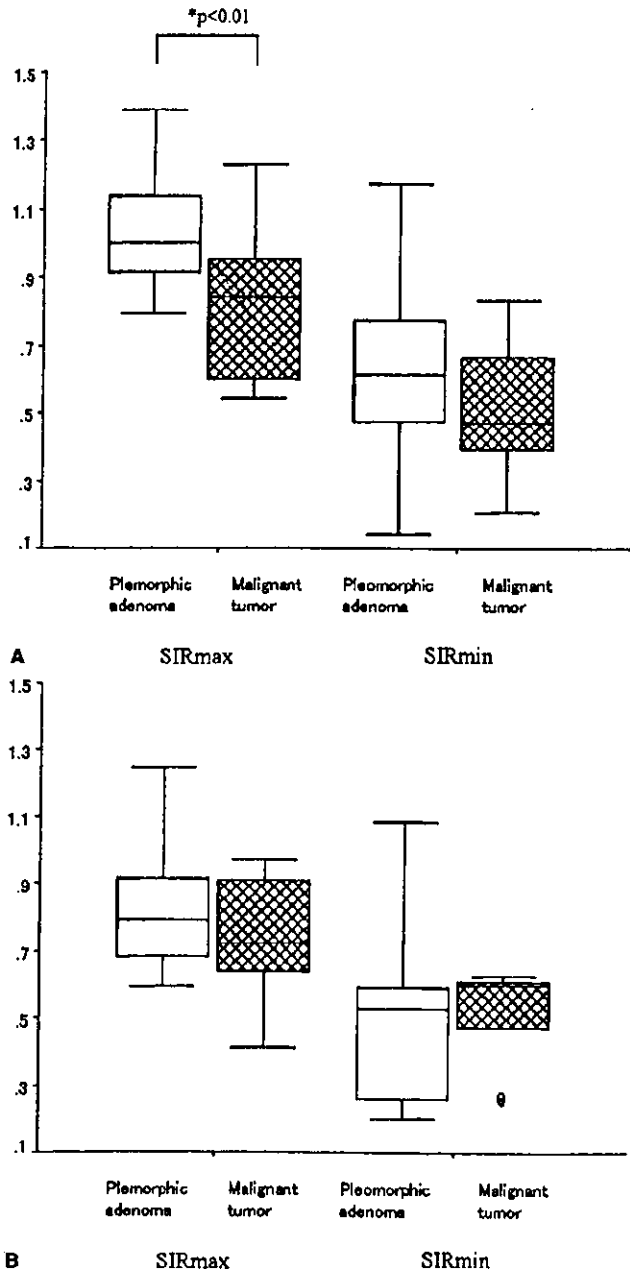

FIGURE 3. A, SIR_{max} and SIR_{min} of pleomorphic adenomas and malignant parotid tumors on STIR. The transverse lines within the boxes represent mean, and the boxes represent SD. The lines through the boxes represent the range of the values. * = P value for comparison of pleomorphic adenomas and malignant tumors. SIR_{max} on STIR of pleomorphic adenomas was significantly higher than those of malignant tumors ($P < 0.01$). B, SIR_{max} and SIR_{min} on T2W images. The transverse lines within the boxes represent mean, and the boxes represent SD. The lines through the boxes represent the range of the values.

TABLE 2. Time Intensity Curves of Tumors on Dynamic MR Imaging

Case No.	Curve Types							
	A	B	C1	C2	C3	C4	D	E
PA1		+(24.5)				+(2.9)	+	
PA2		+(35.0)				+(0.3)	+	
PA3					+(11.6)		+	
PA4					+(3.3)	+(0.3)	+	
PA5				+(11.5)		+(0.6)	+	
PA6	+(17.6)		+(29.8)				+	
PA7							+	
PA8							+	
PA9							+	
PA10							+	
PA11							+	
PA12						+(1.2)	+	
PA13		+(6.3)					+	
PA14							+	
PA15							+	+
PA16		+(22.4)					+	
PA17		+(19.9)					+	
PA18							+	
PA19							+	
PA20				+(3.2)			+	
PA21					+(1.6)		+	
PA22						+(5.1)	+	
PA23							+	
PA24							+	
PA25							+	
PA26	+(11.4)						+	
PA27			+(5.0)				+	
PA28					+(1.4)	+(0.6)	+	
PA29							+	
PA30						+(1.1)	+	
PA31						+(4.6)	· +	
PA32						+(3.5)	+	
PA33	+(18.8)				+(2.6)		+	+
AC1		+(22)						
AC2		+(25)						
AC3		+(20)						+
AC4	+(24)							
ME5	+(38)		+(11)					
ACC6		+(15)					+	
SD7			+(11)	+(6)			+	
SD8							+	
SD9		+(12)						+
SD10							+	
SD11	+(27)						+	
ML12		+(29)						
ML13	+(53)							

PA, pleomorphic adenomas; AC, acinic cell adenocarcinoma; ME, mucoepidermoid carcinoma; ACC, adenoid cystic carcinoma; SD, salivary duct carcinoma; ML, malignant lymphoma.
Washout ratio (WR) in parenthesis, expressed as a percentage.

mum and minimum ADC values of both tumors and the ADC values of spinal cord were measured. The average of the maximum ADC values of these 22 pleomorphic adenomas [2.03 ± 0.32 (SD), 1.47 to 2.51 × 10^{-3} mm²/s] was higher ($P < 0.01$) than that of 16 malignant tumors [1.40 ± 0.39 (SD), 0.80 to 2.10 × 10^{-3} mm²/s] and that of the spinal cord [1.02 ± 0.05 (SD), 0.93 to 1.16 × 10^{-3} mm²/s]. The average of the minimum ADC values of pleomorphic adenomas [1.52 ± 0.30 (SD), 0.94 to 2.08 × 10^{-3} mm²/s] was also higher ($P < 0.01$) than that of malignant tumors [1.01 ± 0.29 (SD), 0.48 to 1.35 × 10^{-3} mm²/s] (Fig. 4).

Correlations Between Radiologic and Pathologic Findings

Pleomorphic Adenomas

All tumors had fibrous capsules at the maximal diameter section. The fibrous capsules varied in thickness, and the tumors were separated from normal major glands, which were sometimes demonstrated by MR images. Characteristic bright intensity areas on STIR and T2W images corresponded to areas with abundant myxoid components. These myxoid com-
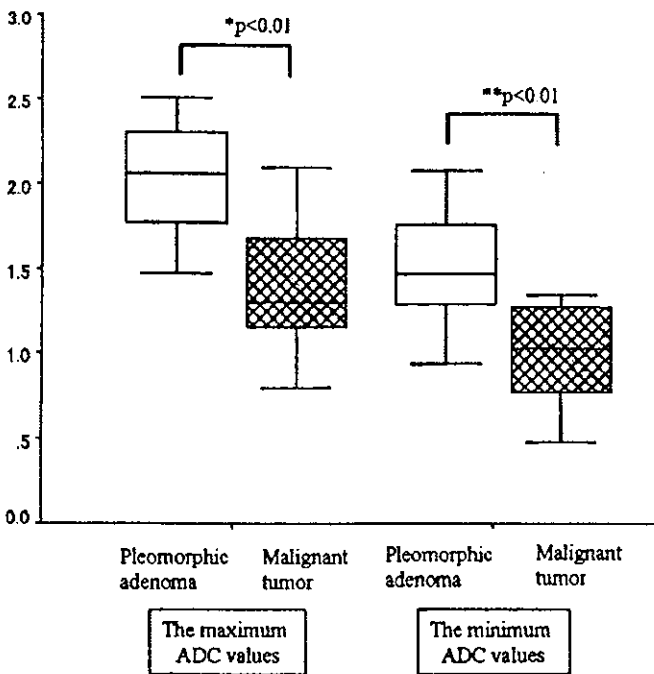

FIGURE 4. The maximum and minimum ADC values of pleomorphic adenomas and malignant parotid tumors on DW images. The transverse lines within the boxes represent mean, and the boxes represent SD. The lines through the boxes represent the range of the values. * and ** = P value for comparison of pleomorphic adenomas and malignant tumors. The maximum ADC values of pleomorphic adenomas were significantly higher than those of malignant parotid tumors, as were the minimum ADC values ($P < 0.01$).

ponents showed progressive enhancing curves (type D) on dynamic MR images and had high ADC values on DW images. On the other hand, areas of hypercellularity and sparse myxoid component did not show the type D perfusion curve. These areas showed a relatively low ADC value compared with those with abundant myxoid components. Cystic areas showed high intensity on STIR and T2W images and high ADC value on DW images without enhancement.

In case 6 (Fig. 5), the tumor had type A curve at the maximal diameter section on the axial plane. This area showed moderately high intensity on STIR. Small regions showing type C1 and D perfusion curves on dynamic MR images and marked high intensity on STIR were located in the most cephalad portion of the tumor. The pathologic specimen from the maximal diameter section revealed hypercellularity and sparse myxoid component.

In case 8 (Fig. 6), all portions of the tumor showed type D perfusion curve on dynamic MR images. On T2W images, this tumor showed marked high intensity, higher than that of CSF. The pathologic specimen revealed abundant myxoid and scattered cellular components.

In case 27 (Fig. 7), there was a hypointensity area at the center of the tumor on STIR and T2W images. The pathologic specimen revealed fibrosis in this area.

In case 33 (Fig. 2), the tumor showed 2 marked high-intensity regions at the maximal diameter section on the axial plane of STIR images. One of them showed nonenhancement on dynamic MR images and had high ADC value (2.51 × 10^{-3} mm²/s) on DW images. The other showed type D perfusion curve on dynamic MR images and also had a high ADC value (1.94 × 10^{-3} mm²/s). The pathologic specimen of the maximal diameter section of the former revealed a cyst containing brown fluid, and the latter contained myxoid tissue. The remainder of this tumor was composed of cellular tissue with some capillary vessels and small wedge-shaped portions of myxoid tissue. This region of predominately cellular tissue showed markedly heterogeneous enhancement on dynamic MR images, and multiple ROIs were obtained. This region had type A and C3 perfusion curves. On DW images, this region had a relatively low ADC value (1.38 × 10^{-3} mm²/s).

Malignant Tumors of Parotid Glands

In a case (AC4 in Table 2) of acinic cell adenocarcinoma (Fig. 8), the small tumor in the right parotid gland showed marked high intensity similar to that of CSF on the axial plane of STIR image and moderately high intensity on the coronal plane of T2W image. The tumor had a well-defined margin and showed type A perfusion curve on dynamic MR images. On DW images, this region had a low ADC value (1.22 × 10^{-3} mm²/s). The pathologic specimen revealed numerous small spaces interspersed among the epithelial tumor cells, representing a microcystic growth pattern of acinic cell adenocarcinoma.
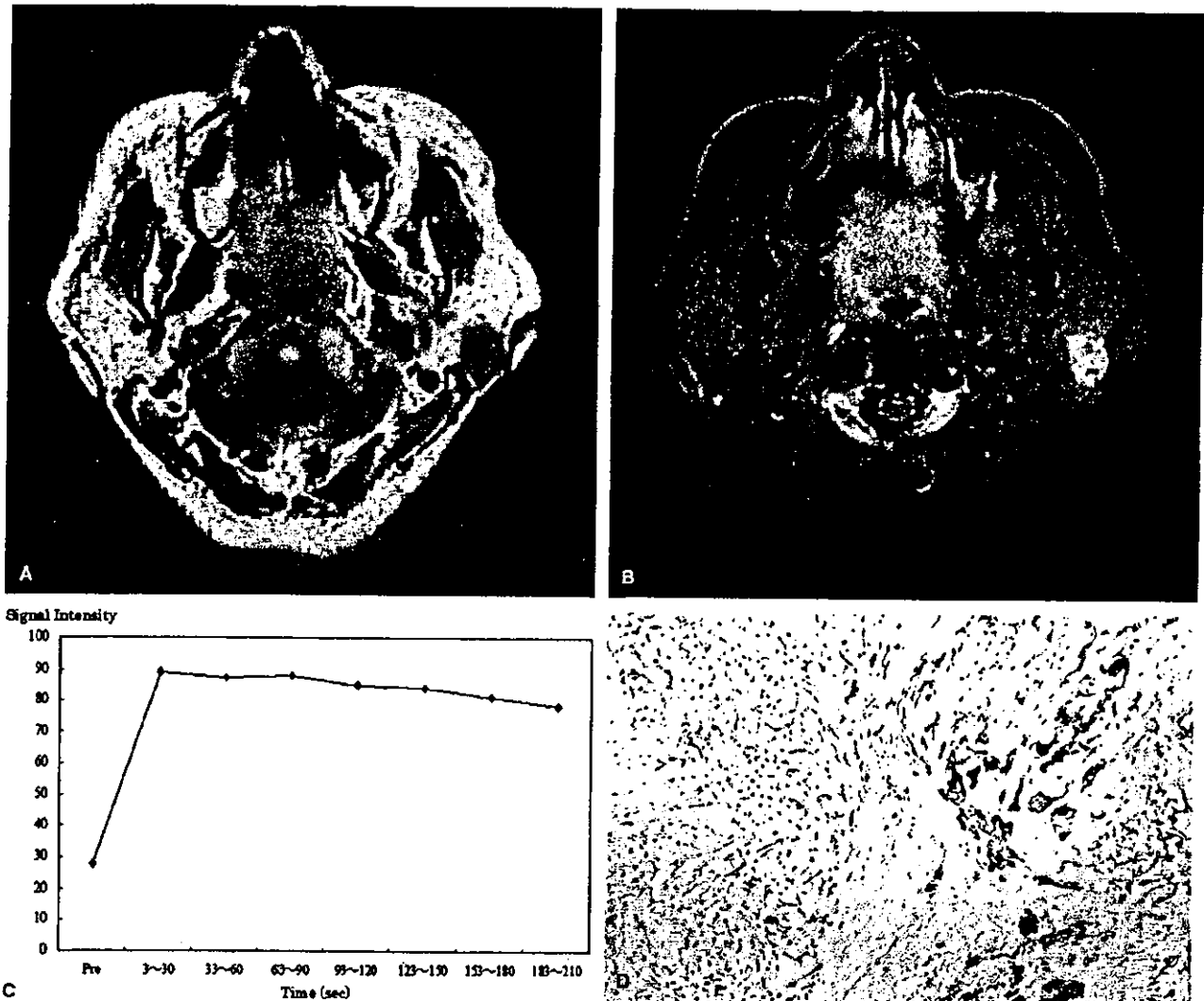
FIGURE 5. Case 6, pleomorphic adenoma in the left parotid gland of a 67-year-old woman. A, T1W image [400/9 (TR/TE), axial plane] of the maximal diameter section shows a lobulated tumor of isointensity for muscle in the superficial lobe. B, STIR image (4000/30, axial plane) shows moderately high-intensity tumor. C, All of the tumor at the same level as T1W and STIR images shows type A perfusion curve on dynamic MR images. D, Maximal diameter axial section of the specimen shows hypercellular and sparse interstitial components.

In a case (ME5 in Table 2) of mucoepidermoid carcinoma (Fig. 9), the tumor in the left parotid gland demonstrated an ill-defined and invasive border. The tumor showed low to moderately high intensity on STIR images, and type A and C1 perfusion curves on dynamic MR images. On DW images, this region had a low ADC value (1.24×10^{-3} mm^2/s). The pathologic specimen revealed a parotid gland tumor in which intracystic space comprised more than 20% of the total area. The tumor was low-grade mucoepidermoid carcinoma without neural invasion or necrosis, and with very few mitoses.

In a case (ACC6 in Table 2) of adenoid cystic carcinoma (Fig. 10), the tumor showed a lobulated and ill-defined margin.

The tumor showed marked high intensity on STIR image, higher than that of CSF. This high-intensity region on STIR image showed type D perfusion curve on dynamic MR images and had a high ADC value (1.68×10^{-3} mm^2/s) on DW image. The remaining region showed type B perfusion curve and had a relatively low ADC value (1.29×10^{-3} mm^2/s). The pathologic specimen revealed myxoid-rich tissue and islands of neoplastic epithelial cells containing several small, round, and pseudocystic structures. This was the cribiform type of adenoid cystic carcinoma.

In a case (SD10 in Table 2) of salivary duct carcinoma (Fig. 11), the margin of the tumor was unclear and invasive.